Werk

Jahr: 1979
Kollektion: fid.geo
Signatur: 8 Z NAT 2148:46
Digitalisiert: Niedersächsische Staats- und Universitätsbibliothek Göttingen
Werk Id: PPN1015067948_0046
PURL: http://resolver.sub.uni-goettingen.de/purl?PPN1015067948_0046

LOG Id: LOG_0020
LOG Titel: Auroral particle fluxes in the ionosphere
LOG Typ: article

Übergeordnetes Werk

Werk Id: PPN1015067948
PURL: http://resolver.sub.uni-goettingen.de/purl?PPN1015067948
OPAC: http://opac.sub.uni-goettingen.de/DB=1/PPN?PPN=1015067948

Contact

Niedersächsische Staats- und Universitätsbibliothek Göttingen
Georg-August-Universität Göttingen
Platz der Göttinger Sieben 1
37073 Göttingen
Germany
Email: gdz@sub.uni-goettingen.de

J. Geophys. 46, 151–169, 1979

Journal of Geophysics

Auroral Particle Fluxes in the Ionosphere

K. Wilhelm

Max-Planck-Institut für Aeronomie, D-3411 Katlenburg-Lindau 3,
Federal Republic of Germany

Abstract. The observations discussed in this paper were conducted in the framework of the 'Polar High Atmosphere Sounding Rocket Project' with a view to determining the contributions of auroral particle fluxes to both the energy budget and the current system of the upper atmosphere. The experiment was flown on board four payloads that were launched into various phases of magnetospheric substorm events to peak altitudes of approximately 270 km. During undisturbed portions of the flight times the electron flux below 500 eV was nearly isotropic and could be described by a power law spectrum. At high energies the spectra were steeper and exhibited a loss signature in the atmospheric backscatter cone. In disturbed periods electron fluxes with peaked spectra in the keV energy range were often superimposed on these distributions. In addition, strongly field-aligned electron fluxes were frequently observed at low energies. It seems difficult to devise any other mechanism to explain some of the observed events than field-aligned electric field acceleration. Results will also be presented on the energy flux carried by electrons and protons and the relationship to optical auroral emissions.

Key words: Magnetospheric substorm – Auroral particle fluxes – Magnetically aligned electric fields.

1. Introduction

The low-energy auroral particle experiment (AL1) was flown on four complex payloads in the framework of the 'Polar High Atmosphere Sounding Rocket Project'. The main goal of the experiment was to determine the bulk properties of low-energy particle fluxes during various phases of magnetospheric substorm events in order to provide input data for interpreting the atmospheric response to magnetospheric disturbances. This response was observed on the ground and by other instruments of the payload compliment comprising plasma experiments, mass spectrometer, magnetometer, and optical instruments. A description

0340-062X/79/0046/0151/$03.80

of the scientific objectives, the payload and the geophysical launch conditions has been given by Theile (1978).

Another scientific objective of the low-energy particle experiment was to study the particle distribution function as a means to deduce particle acceleration and precipitation mechanisms. Low-energy electron fluxes can be considered as sensitive probes of magnetospheric electric fields. In view of the importance of these fields, the data presented here will mainly be considered in the context of possible acceleration and precipitation mechanisms involving electric fields. Other aspects such as energy input into the high atmosphere, electric current distributions and wave-particle interaction processes will have to be treated in more detail, in a later paper together with supporting information from other experiments flown on the payloads or operated elsewhere. All observations discussed here were made over or near auroral forms in various stages of activity. To further the understanding of this exciting phenomenon of the polar night was one of the motivations for performing the measurements. In earlier investigations it has been recognized that the observed spectra can be divided into primary and secondary electron fluxes. Secondary electrons normally have energies of less than 500 eV and tend to be completely isotropic with a power law dependence of the flux and spectral parameters between 1 and 2 (Cahill et al., 1974; Arnoldy et al., 1974; Peterson et al., 1977). This behaviour was theoretically explained by considering the interaction of primary electron beams with the atmosphere by Banks et al. (1974) and by taking into account the reflection of upwards going low-energy electrons at potential barriers that supposedly are located above auroral displays (Evans, 1974).

In the energy range of several keV electron fluxes with peaked energy spectra were often observed above bright auroral displays. It was also recognized that these fluxes were normally field-aligned (O'Brien and Reasoner, 1971; Whalen and McDiarmid, 1972; Arnoldy et al., 1974; Cahill et al., 1974; Boyd, 1975). Mende and Shelley (1976) demonstrated that the spectral peaks could not be correlated with observations on a geosynchronous satellite thus supporting a mechanism of low-altitude post-acceleration of auroral particles. Boyd (1975) arrived at a threshold intensity for peaked spectra of about 12 erg $cm^{-2} s^{-1}$ corresponding to an IBC II aurora. Low-energy electron fluxes have also been identified as being important carriers for magnetospheric electric currents (Arnoldy et al., 1974; Cahill et al., 1974).

2. Instrumentation

The low-energy auroral particle experiment was designed to achieve good energy and angular resolution for electrons and protons. These requirements resulted in a nested-electrostatic analyser system, named differential energy analyser (DEA), followed by continuous channel electron multipliers (CEM) for separate electron and proton detection. A schematic sketch of the analyser is given in Fig. 1. The outer and inner spheres were grounded and the potential of the middle sphere was varied between 0 and -4 kV. Plasma rejection was achieved by a double grid in front of the entrance aperture at ground and

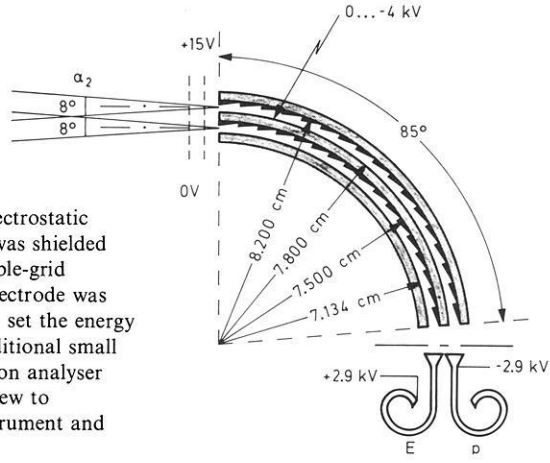

Fig. 1. Schematic sketch of the nested-electrostatic analyser (DEA). The entrance aperture was shielded from thermal plasma particles by a double-grid structure. The potential of the middle electrode was varied between 0 and -4 kV in order to set the energy acceptance band of the analyser. An additional small CEM (e) was mounted behind the electron analyser outside the plane of this figure with a view to increasing the dynamic range of the instrument and providing some redundancy

$+15$ V. As, in general, the rocket skin was at slightly negative potentials of a few Volts with respect to the plasma, both thermal electrons and protons were excluded from the inside of the analyser by this arrangement. The outer channel deflected protons and the inner one electrons into the detection devices. Before entering the CEM, the protons were post-accelerated by a voltage of -2.9 kV to enhance the instrument efficiency for low-energy protons. The concave surfaces were serrated in order to reduce scattering of particles inside the spherical analysers. In addition, the aluminium spheres were chromium-black plated, which, at the same time, guaranteed a good electrical conductivity of the surfaces of the spheres.

Two electron channels with different geometric factors and one proton channel were looking approximately 25 deg off the rocket axis. Another identical detector arrangement was mounted under an angle of 115 deg with respect to the payload axis. The sampling time was 15.8 ms followed by a dead time of 0.2 ms. The calibration procedure applied during the laboratory tests of the instruments has been described by Wilhelm (1979). It can be summarized in Fig. 2 by presenting an example of the relative detector efficiency ε_1 as a function of the particle energy, the azimuthal angle α_2 defined in Fig. 1 and the meridional angle α_1 normal to α_2. The two expressions 'meridional' and 'azimuthal' refer to the payload spin axis and imply a special mounting configuration of the instrument with respect to the payload. Given the nominal direction of the payload axis, i.e., parallel to the local vertical, and the magnetic field vector, it can be seen that the pitch angle resolution is predominantly determined by the acceptance range of the 'meridional' angle. For this reason the angle α_1 was mounted parallel to the meridional plane of the rocket. The evaluation of the calibration led to the instrument characteristics given in Table 1.

Taking into account both the CEM properties and the efficiency as a function of energy, one can perform an absolute conversion of count rates into particle fluxes.

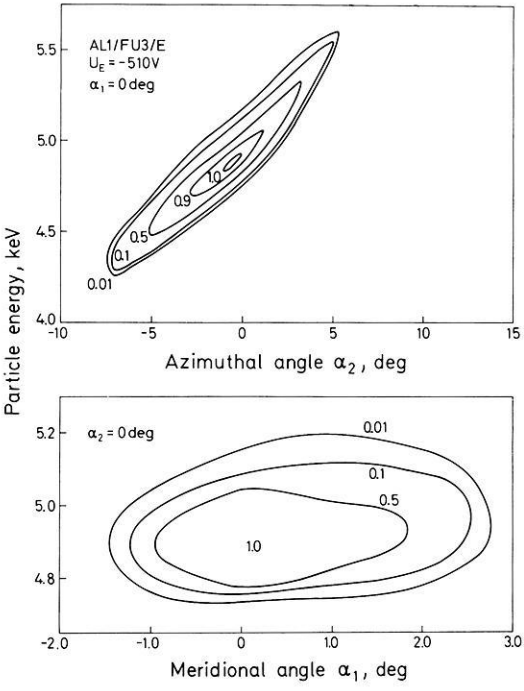

Fig. 2. Contours of the relative efficiency ε_1 of one of the large-geometric-factor electron channels. The efficiency is plotted as a function of the two angular directions and the particle energy. Note the different scales

Table 1. Characteristics of instrument

Energy range,	eV	15–35,000
Resolution $\Delta W/W$,	%	14
Geometric factor,	cm^2 sr	2.3×10^{-3}
Field of view,	deg^2	2.7×8.0
Time resolution,	ms	16
Payload spin period,	ms	330

3. Observations

Four payloads were launched from the Andoya Rocket Range, Andenes, Norway by Skylark 7 motors. A compilation of the launch times and the geophysical conditions encountered is given in Table 2. For details the reader is referred to the description of the project by Theile (1978).

Table 2. Launch times and geophysical conditions

Flight	Payload designation	Launch time (GMT)		Apogee (km)	Geophysical conditions
1	F2A	January 22, 1977	21:28:00	276.8	Pre-breakup phase
2	F1B	February 8, 1977	22:11:51	272.7	Active auroral display
3	F3C	February 20, 1977	21:14:00	256.0	Quiet diffuse aurora
4	F4D	March 16, 1977	22:04:40	259.3	Active auroral display

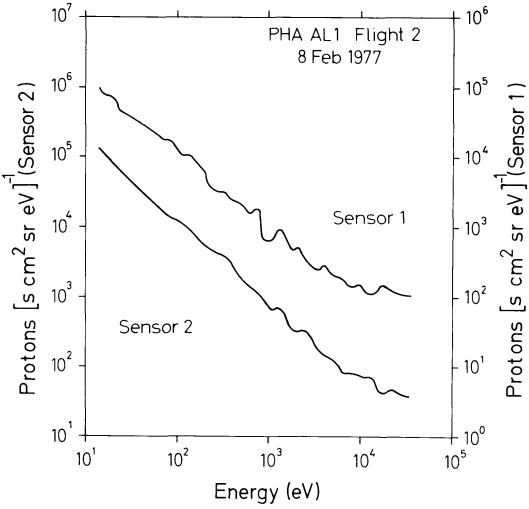

Fig. 3. Proton spectra observed during the second flight (F1B) above an altitude of 250 km. The graphs define an upper limit for the proton observations for fluxes below an energy of several keV. *Sensor 1* covered the upper halfsphere, whereas *sensor 2* mainly looked downwards. Notice that the scales for the two sensors are displayed by a factor of 10

With two exceptions the payloads performed nominally as far as the requirements of the low-energy particle experiment were concerned. A spin-modulated telemetry loss occurred during the later portions of the first flight (F2A) and payload 3 (F3C) was exposed to humidity during ground handling procedures resulting in an unacceptable dark count rate in one sensor system that, as a consequence, had to be disconnected before launch. All the other channels worked according to expectation. The pitch angle scans of the two sensor heads were rather restricted due to the stabilisation of the payloads under nominal conditions. In this sense, an accidentally induced high coning angle on the second flight (F1B) was profitable for this experiment.

Proton Flux Observations. The proton fluxes measured during all flights were very low and did not permit any significant time history study. The measurements can be summarized in two representative spectra that are given in Fig. 3. They have been produced by integrating all the proton measurements above 250 km during the second flight (F1B) separately for both directional channels. Taking the count statistics and the noise levels of the detectors into account, the spectra can only be regarded as significant above several keV proton energy. Below that energy, it can be concluded that the flux levels stayed below the threshold sensitivities of the detectors represented by the graphs.

Electron Distributions. Measurements of electron energy spectra will conveniently be displayed either as differential electron flux $F(\alpha, W)$ in units of electrons $\mathrm{cm}^{-2}\,\mathrm{s}^{-1}\,\mathrm{sr}^{-1}\,\mathrm{eV}^{-1}$ assuming azimuthal symmetry around the magnetic field direction or as velocity distribution function $f(\mathbf{v})$ in $\mathrm{s}^3/\mathrm{km}^6$ in order to study some of their characteristics. The symbols α, W, and $\mathbf{v}$ denote electron pitch angle, energy and velocity vector, respectively. The electron flux and the velocity distribution function are related by

$$f_e(\mathbf{v}) = m_e^2 F(\alpha, W)/2W \tag{1}$$

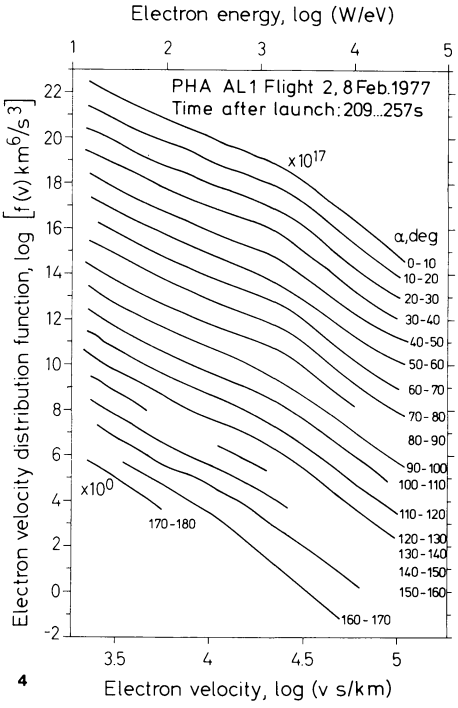

Fig. 4. Electron velocity distribution function plotted versus electron velocity (and energy) with pitch angle ranges as parameter. The format of the presentation allows 18 pitch angle ranges of 10 deg width each to be displayed by displacing the curves by a factor of 10 with respect to each other. The scale is given for the 170–180 deg curve. The observation were made in the time interval from 209 ... 257 s after launch of flight 2 (F1B). The instrument was looking upwards along the field line when 0 deg pitch angle particles were observed

with m_e the electron mass and $W = m_e v^2/2$ the non-relativistic electron energy. It will first be attempted to illustrate the normal electron velocity distribution function that was observed for most of the flight times. A typical observation is shown in Fig. 4. Characteristic for this distribution is a knee at approximately 3×10^4 km/s corresponding to $W \approx 2$ keV with a steep decrease to higher velocities. The differential energy spectrum of this distribution can be described by two power law functions as

$$F \propto W^{-\gamma} \tag{2}$$

with

$$\gamma = 1.0 \quad \text{for } W < 2\,\text{keV}$$

and

$$\gamma = 2.2 \quad \text{for } W > 2\,\text{keV}.$$

Except for a loss cone signature at high velocities the distribution is more or less isotropic in the range covered by the observations.

Near bright auroral arcs the distribution was similar but the knee shifted to higher velocities, the high-energy slope steepened and a plateau or a relative maximum developed below the knee velocity. Illustrations of this type of distribution are given in Figs. 5 and 6 in terms of the electron distribution

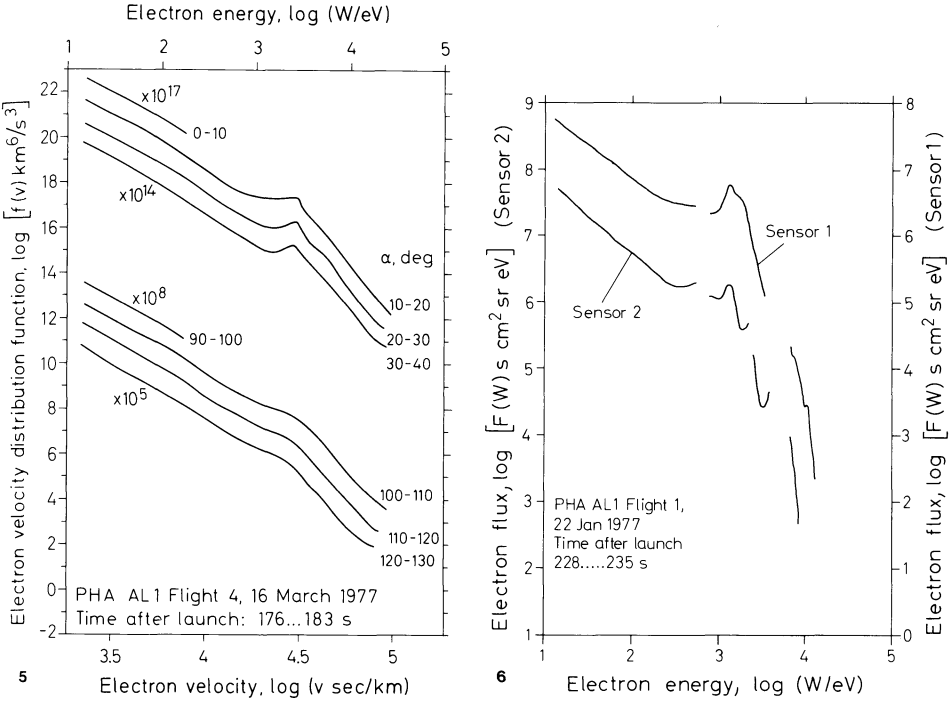

Fig. 5. Electron velocity distribution function between 176 ... 183 s after launch of F4D. For details of the format see Fig. 4. Due to the limited pitch angle coverage only 8 ranges are available for F4D

Fig. 6. Differential electron flux versus energy measured during the time interval from 228 ... 235 s on the first flight (F2A). The gaps result from data losses caused by the telemetry failure mentioned in Sect. 3. The *sensors 1 and 2* scanned pitch angle ranges of 0 to 40 and 90 to 130 deg, respectively

function and the differential energy spectrum. The fluxes exhibit field-aligned collimation near the peak intensities. Predominantly north of the auroral displays the distributions were more complex as can be seen from Fig. 7. Again the knee signature near 2 keV electron energy is present but, in addition, another change of slope of the velocity distribution function can be detected near 200 eV. Similar to the simple distribution in Fig. 4, it is typical for the double knee distribution that the electron fluxes are nearly isotropic, although a tendency of field-alignment can be noticed at low energies. Distributions such as those in Figs. 4 and 7 can be looked at as reference distributions. Superimposed on them, strongly field-aligned electron fluxes were observed on many occasions that exhibited a marked difference in their characteristics to the reference distributions. Figure 8 illustrates one of these events in terms of the differential energy flux in two different pitch angle ranges. The apparent spin modulation between 0.2 and 2 keV with peak fluxes near 0 deg pitch angle is the instrumental response to strongly field-aligned electron precipitation within this wide energy range. The degree of alignment can best be seen in flux versus pitch angle plots given in Fig. 9 for another event having similar features. For still

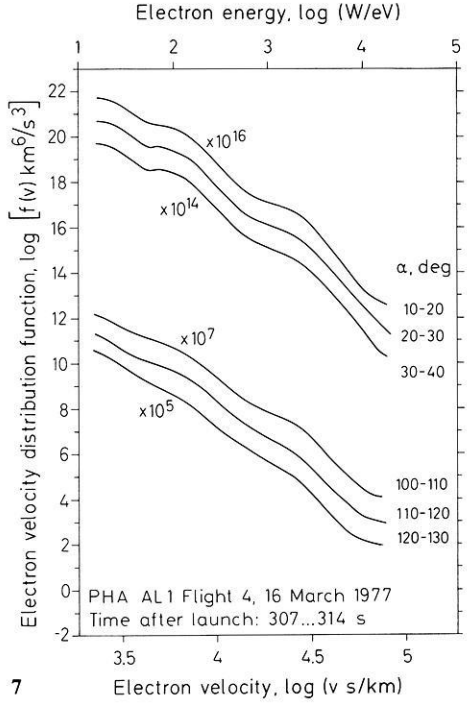

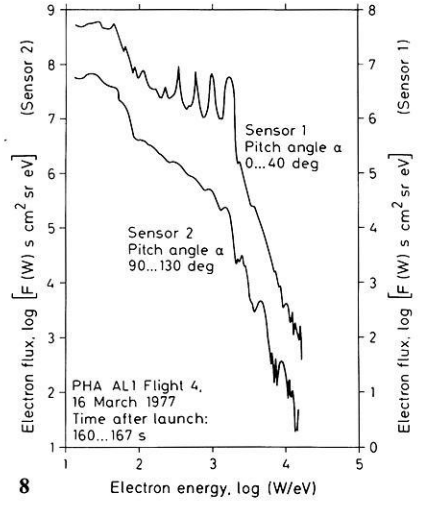

Fig. 7. Electron velocity distribution function observed from 307... 314 s after launch of F4D. For details see Fig. 4

Fig. 8. Electron differential energy spectra measured in two pitch angle ranges on F4D between 160 ... 167 s elapsed time

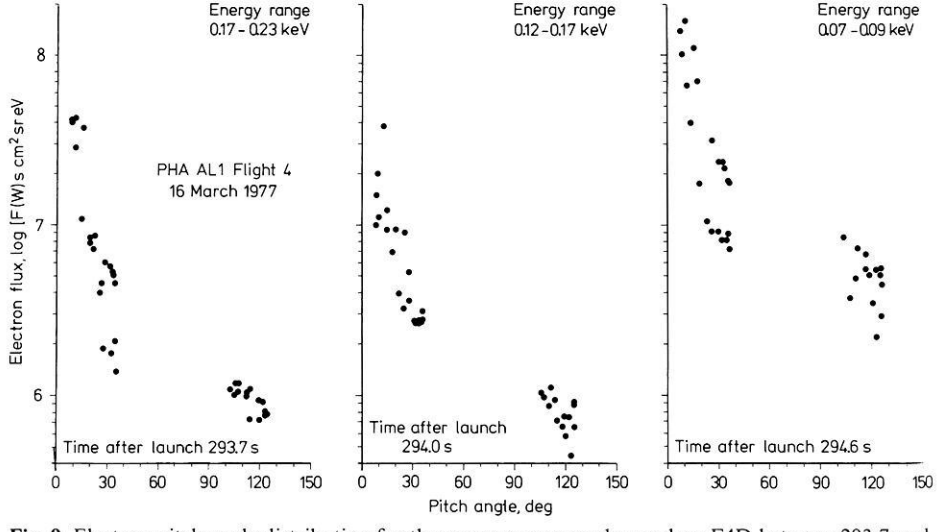

Fig. 9. Electron pitch angle distribution for three energy ranges observed on F4D between 293.7 and 294.6 s elapsed time

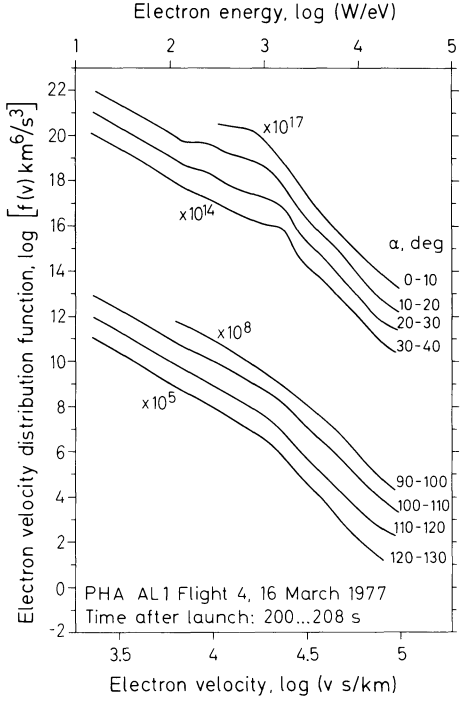

Fig. 10. Electron velocity distribution function in the time period from 200 ... 208 s after launch of F4D. For details see Fig. 4

another event the velocity distribution function has been plotted in Fig. 10 demonstrating that a pronounced density increase at small pitch angles is characteristic for this type of event. Moreover it should be noted that the increase is situated at velocities smaller than the knee velocity. Field alignment of the electron flux was present as low as $v = 8.4 \times 10^3$ km/s ($W = 200$ eV) in this example but could be observed down to $v = 3.2 \times 10^3$ km/s ($W = 30$ eV) on other occasions. Considering the low altitude at which the measurements were made and the mean free path length of the order of 10 km for the low-energy electrons involved, the existence of such strongly field-aligned fluxes is highly surprising and merits detailed investigations.

The knee distributions were very stable in time. The field-aligned events, on the contrary, exhibited a burst-like-structure with a duration of several seconds for individual events. With a view to understanding the causes of these events with strong field alignment of the electron flux, part of the data of Fig. 10 have been reorganized as contours of constant distribution functions in velocity space in Fig. 11. The solid lines represent those regions in velocity space that were directly observed by the instrument. The broken lines are interpolations believed to be possible without ambiguity. There are several interesting features that should be noted in Fig. 11:

– in the first quadrant the distribution function contours for energies greater than 2 keV are nearly circular;

– a loss cone effect is present for pitch angles greater than 105 deg in the second quadrant, corresponding to a local loss cone angle of 75 deg;

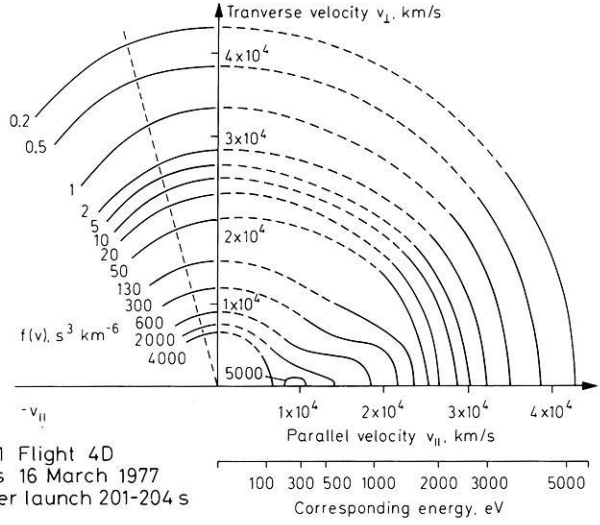

Fig. 11. Constant electron distribution function contours in velocity space. In addition to the velocity scales, the corresponding energy of electrons is given. *Left of the dashed line*, intensity decreases can be seen caused by loss cone effects. The distrition was measured on F4D between 201–204 s elapsed time

– the field-aligned event clearly stands out along the $+v_\parallel$ axis with a relative maximum at $v \approx 10^4$ km/s.

Electron Number and Energy Fluxes. In order to arrive at the bulk properties of the electron flux, the differential electron flux $F(\alpha, W)$ can be integrated to give the number and energy flux densities according to

$$n_{\text{down}} = 2\pi \int_0^{\pi/2} \int_{W_1}^{W_2} F(W, \alpha) \sin\alpha \cos\alpha \, dW d\alpha \tag{3}$$

$$Q_{\text{down}} = 2\pi \int_0^{\pi/2} \int_{W_1}^{W_2} WF(W, \alpha) \sin\alpha \cos\alpha \, dW d\alpha \tag{4}$$

Similarly, the upwards going fluxes can be determined. The electric current density carried by electrons in the energy range under consideration then follows from the difference of the two opposite number flux densities. As the instrumental conditions differed for all four flights, a separate discussion is required in each case.

Starting with the second flight (F1B), it should be recalled that the large coning angle of the payload was favourable as far as a complete pitch angle scan of this instrument was concerned. However, as another consequence, the time resolution was substantially deteriorated. Fortunately, time variations of the electron flux were not very pronounced during this flight, thus allowing a long integration time without serious implications. The results are presented in Fig. 12. Optical observations showed that the payload was engulfed in auroral

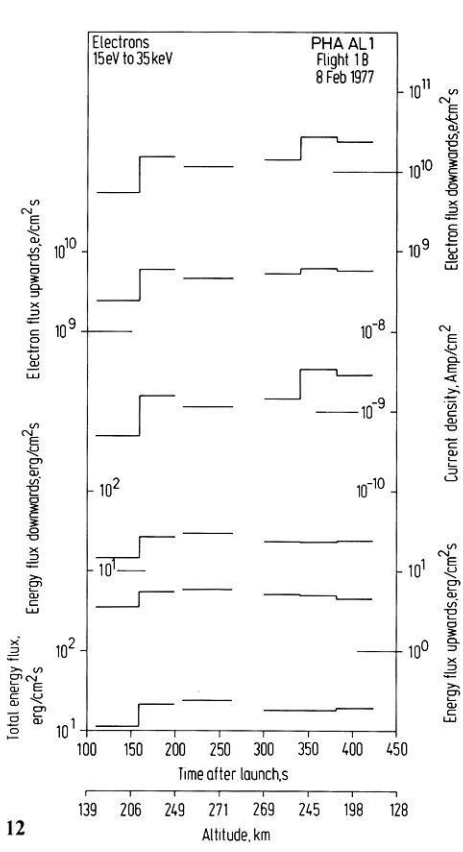

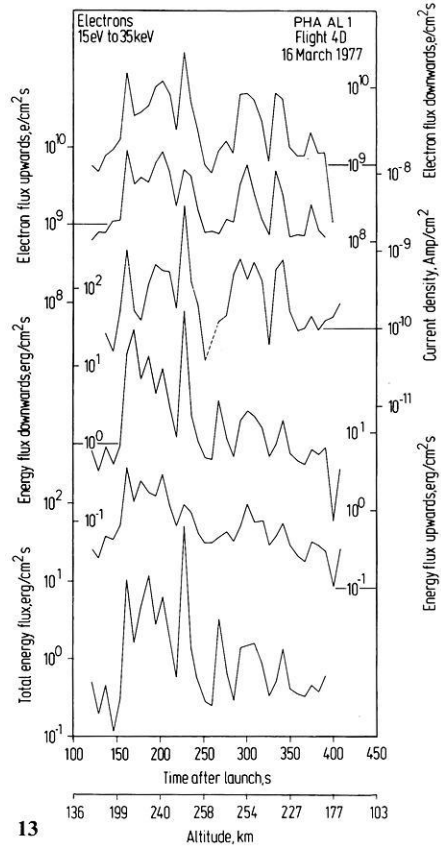

Fig. 12. Electron flux parameters for the second flight (F1B) on February 8, 1977. The upper three histograms show the electron flux densities and the lower ones indicate the corresponding energy fluxes. Time variations of the electron flux in certain intervals prevented long integration times and consequently no flux densities and energy fluxes could be computed

Fig. 13. Electron flux parameters for the fourth flight (F4D) on March 16, 1977

activity with an intensity of 3 to 4 kR at 557.7 nm for all of the flight time (Theile, private communication).

On the fourth flight (F4D), the pitch angle scan was restricted to intervals of 2×40 deg. Before the integration of Eqs. (3) and (4) could be performed, inter- and extrapolation methods had to be used following a procedure discussed by Wilhelm (1979). It was shown that the computations could be considered with confidence for spectra with reasonably smooth behaviour. In Fig. 13 the results of F4D have been compiled. The dramatic increase of all quantities between approximately 150 and 240 s elapsed time coincided with the encounter of the payload with the visible auroral are as can be seen from Fig. 14 where the intensities contours derived from 557.7 nm scanning photometer measurements have been plotted as a function of time and geographic location.

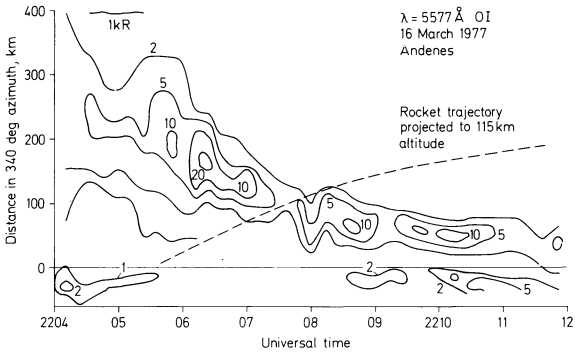

Fig. 14. Photometer observations of the 557.7 nm oxigen line during the flight time of F4D. The scan was performed in the 340 deg azimuth plane corresponding to the launch directions of the sounding rocket. The trajectory of the payload projected down to 115 km altitude has also been included

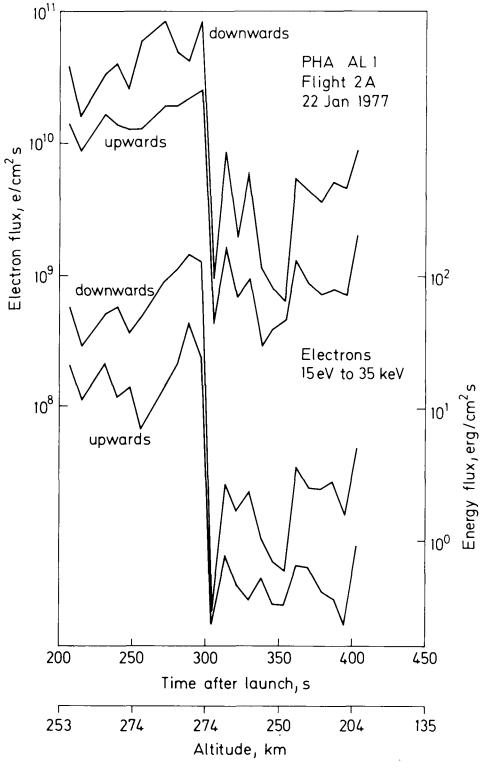

Fig. 15. Electron flux parameters for the first flight (F2A) on January 22, 1977

The technical limitations prohibited a numerical evaluation for both the third (F3C) and the first (F2A) flight. Graphical methods were therefore used that could only provide an estimate of the quantities under consideration. The results have been displayed in Fig. 15 for F2A. Of particular interest seems to be the decrease near 300 s after launch. Even if the uncertainties in absolute values

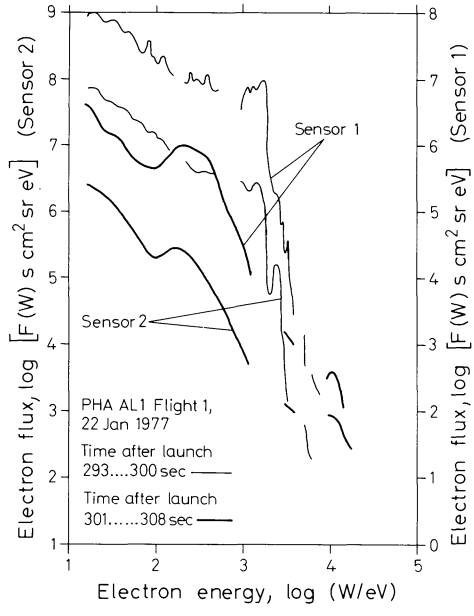

Fig. 16. Electron energy spectra before and after the flux intensity decrease at 300 s elapsed time on F2A

should be considerable, the relative decrease of more than two orders of magnitude in energy flux can be considered as genuine. The spectra before and after that discontinuity have been plotted in Fig. 16.

4. Discussion

There is increasing evidence supporting the hypothesis that magnetospheric charged particles are being accelerated or post-accelerated near the ionosphere before they precipitate into the atmosphere (Maehlum and Moestue, 1973; Evans, 1974; Mozer, 1976; Raitt and Sojka, 1977; Bryant et al., 1978; Mizera and Fennell, 1977). The signature of electron distributions should be a sensitive indicator of fieldaligned static electric field acceleration as was discussed by Whipple (1977) for natural and Wilhelm (1977) for artificially injected particles. Under the assumption of adiabatic motion, equivalent to the constancy of the magnetic moment

$$\mu = \{W_0 - q[\phi(s) - \phi(s_0)]\} B^{-1}(s) \sin^2 \alpha \qquad (5)$$
$$= m_e v_\perp^2(s)/2B(s) = \text{const}$$

with

W_0 initial kinetic energy
q charge of particle
$\phi(s)$ electric potential at position s
$B(s)$ magnetic field strength at s
$v_\perp(s)$ perpendicular velocity with respect to the magnetic field at s

the main conclusion was that the presence of an accelerating electric field parallel to the magnetic field would subdivide the particle population into several distinct regimes in velocity-space. The identification of these regimes and the corresponding boundaries in the observed particle distributions should thus be indicative of the operation of the assumed mechanisms. Chiu and Schulz (1978) have given a full description of the different phase space regimes and the corresponding demarcation lines. Using their analysis, Croley et al. (1978) have pointed out that the region in velocity space which defines the trajectories of charged particles that are turned around by an electric field above the point of observations s_1 is given by the interior of the ellipse

$$v_{\parallel}^2(s_1)+[1-B(s_0)\,B^{-1}(s_1)]\,v_{\perp}^2(s_1)=-2\,q\,\phi(s_1)/m_e \tag{6}$$

with $v_{\parallel}(s_1)$ parallel velocity with respect to the magnetic field at s_1 and $B(s_0)$ magnetic field strength where the potential function ϕ vanishes.

Similarly, the loss of particles in the atmosphere at the position s_2 can be projected upwards by

$$v_{\parallel}^2(s_1)+[1-B(s_2)\,B^{-1}(s_1)]\,v_{\perp}^2(s_1)=2q\,[\phi(s_2)-\phi(s_1)]/m_e \tag{7}$$

resulting in a region bounded by a hyperbola at the altitude of observation s_1. Furthermore, Croley and co-workers have presented an example of electron flux measurements in their Fig. 1b that showed, except for the loss cone effect, circular contour lines for $v>1.87\times10^4$ km/s and a sharp demarcation line at that velocity. They interpret these findings as evidence of a field-aligned electrostatic acceleration of magnetospheric electrons in a potential drop of 1 kV above the satellite. The circular domain boundary could be described by Eq. (6) under the assumption of $B_0 \ll B(s_1)$, i.e., a rather high upper limit of the electric field region.

The observations presented in Fig. 11 of this paper resemble those discussed above to a high degree for electron velocities greater than 2.5×10^4 km/s. Similarly, it can be seen from Figs. 5 and 6 that presentations of the same data in velocity space would result in circular demarcation lines at velocities near 3×10^4 km/s. As far as the high-velocity electrons are concerned, the measurements obtained during the time periods discussed are thus consistent with an electrostatic field acceleration. It can, therefore, be concluded that the distribution shown in Figs. 5 and 6 are indicative of a field-aligned acceleration process operating at great altitudes. All electrons with velocities greater than the knee velocity were of magnetospheric origin and fell through the total potential drop. Electrons with small velocities, on the other hand, belonged to an ionospheric population unable to surmount the potential barrier above the point of observation as suggested by Evans (1974).

The distribution shown in Fig. 7 exhibits a double knee structure and, transferred into velocity space contours, could be characterized by two circular boundaries. As an explanation it is suggested that the cause be sought in two spatially separated electric field regions along the field line of observation. High-velocity electrons were of magnetospheric origin and experienced both acceleration steps, low-velocity ionospheric electrons were reflected by the low-

altitude field, whereas electrons with intermediate velocities originated from the region between the potential gradients.

The ionospheric population consisting of secondary and degraded primary electrons (Banks et al., 1974) was in most cases observed to be rather uniform and, in particular, did not indicate any distinction between particles trapped between the electric field region and the magnetic mirror point and reflected ones. This is in contrast to the findings of Croley and co-workers and might be explained by the low height of the sounding rocket observing point compared to the satellite altitude of several thousand kilometres. The most important difference between the satellite observations as presented by Croley et al. (1978) and the sounding rocket measurements, however, manifests itself in the field-aligned electron flux at ionospheric altitudes. An understanding of this signature of the electron distributions can be achieved by generalising the analysis by Croley and co-workers and modifying the model calculations of Kaufmann et al. (1976) as follows:

For simplicity, a Maxwellian distribution with temperature T and density n_e will be assumed above the electric field region at a station s_0 along the magnetic field line

$$f_e = n(m_e/2\pi kT)^{3/2} \exp(-W_0/kT) \tag{8}$$

where $W_0 = m_e\,[v_\parallel^2(s_0) + v_\perp^2(s_0)]/2$ is the initial energy of a given particle. Constant f_e contours thus are circles in velocity space with radii

$$r_0 = (2W_0/m_e)^{1/2} \tag{9}$$

The question at hand is, how contours of constant f_e project downwards to station s_1 in a converging magnetic field configuration with an accelerating potential gradient. It can immediately be seen from

$$\begin{aligned} v_\parallel^2(s_1) + v_\perp^2(s_1) &= 2\{W_0 - q[\phi(s_1) - \phi(s_0)]\}/m_e \\ &= r_1 \end{aligned} \tag{10}$$

and Liouville's theorem that again circles with radii r_1 describe the resulting projection. It has, however, to be noted that the maximum of $v_\perp$ at s_0 equals r_0 of Eq. (9). As a consequence of the adiabatic assumption in Eq. (5), there exists, independent of the constraint resulting from Eq. (10), a maximum for $v_\perp(s_1)$, namely

$$\mathrm{Max}\,[v_\perp(s_1)] = r_0\,[B(s_1)\,B^{-1}(s_0)]^{1/2} \tag{11}$$

Combining Eqs. (10) and (11), an essential distinction can be defined by

$$\mathrm{Max}\,[v_\perp(s_1)] \gtrless r_1. \tag{12}$$

If, as case 1, both sides are equal, a one-to-one map of the object circle onto the image circle is involved. If, in case 2, the maximum of $v_\perp(s_1)$ is greater than r_1, portions of the object circle are projected on the full image circle. Particles populating the remaining parts of the object circle have no access to the altitude

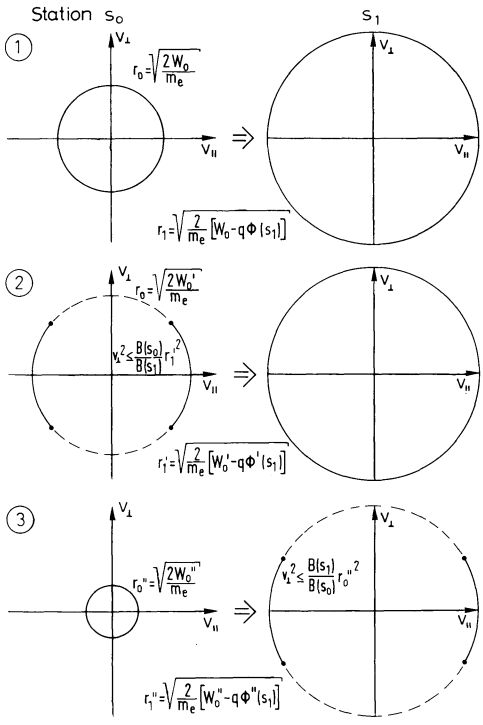

Fig. 17. Schematic illustration of projections in velocity space for the three different cases discussed in the text. In this figure, it was assumed that ϕ vanishes at s_0

of observation as their magnetic mirror points lie above that height. Should, finally, as case 3, the left-hand side be smaller than the radius r_1, the complete object circle would be mapped into portions of the image circle. The three cases are demonstrated in Fig. 17 assuming three different initial energies and specific acceleration potentials. Atmospheric loss processes have not been taken into account in this schematic diagram. Mapping of Eq. (8) under case 3 assumptions for the energy range $0 \leqq W \leqq W_0$ will thus result in an area in velocity space similar to a crescent moon that is bounded by the ellipse of Eq. (6) and the circle of Eq. (10) with $\phi(s_0)=0$.

By rewriting Eq. (12) one obtains

$$B(s_1)\,B^{-1}(s_0)-1 \gtrless -q\,[\phi(s_1)-\phi(s_0)]\,W_0^{-1} \tag{13}$$

The right-hand side is the ratio of the acceleration energy to the initial energy of an electron, whereas the left side can be regarded as a measure of the acceleration distance along the field line. Applying these projections to magnetospheric Maxwellian electron populations, it can be concluded that concentric circles would be observed as constant distribution graphs around the origin, if either the accelerating potential was small compared to the initial energy or the distance along the field line was very long. Conversely, crescentlike projections would be generated when the opposite statements should be true.

As was already discussed, most of the observed constant distribution diagrams contain concentric circular contours with distinct demarcation lines and loss cone effects at high velocities. In the light of the foregoing discussion, this signature suggests, consistent with the conclusion reached earlier, an electrostatic acceleration of hot magnetospheric electrons down to the observing point.

Field-aligned distributions such as that in Fig. 11 have quite frequently been observed superimposed on the more regular distributions. It should be noted that they are characterized by a broad maximum over a wide range in parallel velocity sharply confined to small perpendicular velocities. It is clear that this is the velocity space region that would be occupied by case 3 projections. The wide range in parallel velocity, however, precludes the assumption that all electrons have been accelerated by the total potential drop. Bryant et al. (1978) suggested a time-dependent acceleration or energy dissipation process in order to explain the high flux values at energies below the peak of the spectrum. The measurements presented here confirm earlier observations that these fluxes cannot readily be understood by the reflection model of Evans (1974). However, no indication of fast varying precipitation could be detected either given the time resolution of this experiment. In a simple model it might be assumed that thermal electrons inside the electric field region can under certain conditions be accelerated as well. In accordance with their point of origin these run-away electrons (Mozer, 1976) only gain the corresponding portion of energy giving rise to the extended range in energy observed for these field-aligned events. If, in addition, the temperature of the source plasma was sufficiently low or if the starting point of the acceleration occurred sufficiently near the observing site, the perpendicular velocities would be restricted as required for field-aligned precipitation events. As an abundant supply of cold electrons can only be expected to be available in or near the ionosphere, both conditions point to a local electric field acceleration.

The lack of significant low-energy proton fluxes observed on all four flights might be considered as another indication of electric field acceleration. Even taking into account the effects of charge exchange in the atmosphere that would have neutralized more than 90% of a 2 keV primary proton beam before reaching the detector system (Miller and Whalen, 1976), the measurements support the existence of a strongly selective acceleration process. The restricted pitch angle coverage on the three flights 2A, 3C, and 4D unfortunately prevented the decisive observation of upwards streaming protons as a consequence of a local parallel electric field.

In this context, it is also interesting to study the abrupt changes in the bulk properties of the electron flux. In particular, the sharp decrease at 300 s elapsed time of flight 2A in Fig. 15 suggests that the detector encountered a completely different electron population. On the basis of the optical observations it was concluded that the variation could be interpreted as a spatial structure that was transversed by the payload. Given this dramatic change, it is surprising to note that the electron energy spectra before and after the decrease shown in Fig. 16 can approximately be derived from the same distribution function by an accelerating potential of 0.25 and 1.5 kV, respectively, at least for energies above the peak fluxes.

Field-aligned electron fluxes in the ionosphere led Raitt and Sojka (1977) to the conclusion that local electrostatic field acceleration would be consistent with their observations. They considered atmospheric interactions of the electrons and argued that the degree of alignment observed could not be explained without local acceleration or post-acceleration. The observed and calculated pitch angle distribution did, however, not exhibit the steep increase near 0 deg shown in Fig. 9. Without detailed discussion of the prevailing geophysical conditions, it appears to be difficult to decide whether or not the effects of the same process have been detected in both investigations. Nevertheless, it can be concluded that an electrostatic electric field acceleration process in or near the ionosphere is able to explain a variety of observations and thus is a strong candidate for causing field-aligned auroral electron precipitation.

Acknowledgements. The contributions of C. Becker, R. Schmidt, and W. Engelhardt during the instrument development and operation phases are greatly acknowledged. I thank H.-J. Müller and H.J. Baur for their assistance in the data analysis. The experiment was financially supported by the German Bundesministerium für Forschung und Technologie through DFVLR-PT under grant No. RV 14 - B 112/73 - AI/AL 1.

References

Arnoldy, R.L., Lewis, P.B., Issaacson, P.O.: Field-aligned auroral electron fluxes. J. Geophys. Res. **79**, 4208–4221, 1974

Banks, P.M., Chappell, C.R., Nagy, A.F.: A new model for the interaction of auroral electrons with the atmosphere: Spectral degradation, backscatter, optical emission, and ionization. J. Geophys. Res. **79**, 1459–1470, 1974

Boyd, J.S.: Rocket-borne measurements of auroral electrons. Rev. Geophys. Space Phys. **13**, 735–740, 1975

Bryant, D.A., Hall, D.S., Lepine, D.R.: Electron acceleration in an array of auroral arcs. Planet. Space Sci. **26**, 81–92, 1978

Cahill, L.J., Potter, W.E., Kintner, P.M., Arnoldy, R.L., Choy, L.W.: Field-aligned currents and the auroral electrojet. J. Geophys. Res. **79**, 3147–3154, 1974

Chiu, Y.T., Schulz, M.: Self-consistent particle and parallel electrostatic field distributions in the magnetospheric-ionospheric auroral region. J. Geophys. Res. **83**, 629–642, 1978

Croley, D.R., Mizera, P.F., Fennell, J.F.: Signature of a parallel electric field in ion and electron distribution in velocity space. J. Geophys. Res. **83**, 2701–2705, 1978

Evans, D.S.: Precipitating electron fluxes formed by a magnetic field aligned potential difference. J. Geophys. Res. **79**, 2853–2858, 1974

Kaufmann, R.L., Walker, D.N., Arnoldy, R.L.: Acceleration of auroral electrons in parallel electric fields. J. Geophys. Res. **81**, 1673–1682, 1976

Maehlum, B.N., Moestue, H.: High temporal and spatial resolution observations of low energy electrons by a mother-daughter rocket in the vicinity of two quiescent auroral arcs. Planet. Space Sci. **21**, 1957–1967, 1973

Mende, S.B., Shelley, E.G.: Coordinated ATS 5 electron flux and simultaneous auroral observations. J. Geophys. Res. **81**, 97–110, 1976

Mizera, P.F., Fennell, J.F.: Signatures of electric fields from high and low altitude particles distribution. Geophys. Res. Lett. **4**, 311–314, 1977

Miller, J.R., Whalen, B.A.: Characteristics of auroral proton precipitation observed from sounding rockets. J. Geophys. Res. **81**, 147–154, 1976

Mozer, F.S.: Anomalous resistivity and parallel electric fields. In: Magnetospheric particles and fields, B.M. McCormac, pp. 125–136. ed.: Dordrecht-Holland: D. Reidel Publ. Comp. 1976

O'Brien, B.J., Reasoner, D.L.: Measurements of highly collimated short-duration bursts of auroral electrons and comparison with existing auroral models. J. Geophys. Res. **76**, 8258–8278, 1971

Peterson, W.K., Doering, J.P., Potemra, T.A., McEntire, R.W., Bostrom, C.O., Hoffman, R.A., Janetzke, R.W., Burch, J.L.: Observations of 10-eV to 25-keV electrons in steady diffuse aurora from Atmosphere Explorer C and D. J. Geophys. Res. **82**, 43–47, 1977

Raitt, W.J., Sojka, J.J.: Field-aligned suprathermal electron fluxes below 270 km in the auroral zone. Planet. Space Sci. **25**, 5–13, 1977

Theile, B.: Initial results of the sounding rocket campaign 'Polar High Atmosphere', European Space Agency SP-135, pp. 113–118, 1978

Whalen, B.A., McDiarmid, I.B.: Observations of magnetic-field-aligned auroral electron precipitation. J. Geophys. Res. **77**, 191–202, 1972

Whipple, E.C. Jr.: The signature of parallel electric fields in a collisionless plasma. J. Geophys. Res. **82**, 1525–1531, 1977

Wilhelm, K.: Remote sensing experiment for magnetospheric electric fields parallel to the magnetic field. J. Geophys. **43**, 731–750, 1977

Wilhelm, K.: Beobachtungen von suprathermischen Polarlichtteilchen, Bundesministerium für Forschung und Technologie, Forschungsbericht W 79-03, 1979

Received February 7, 1979; Revised Version June 11, 1979; Accepted June 30, 1979